

RESEARCH ARTICLE

[View Article Online](#)  
[View Journal](#) | [View Issue](#)



Cite this: *Inorg. Chem. Front.*, 2024, **11**, 85

## Direct coupling of two inert CO<sub>2</sub> molecules to form a C–C bond on the Cu<sup>0</sup> atomic interfaces of the nitrogen-doped graphene-supported Cu<sub>4</sub> cluster†

Xin-Jia Cui,<sup>a</sup> Yong-Qing Qiu,<sup>b</sup> Hong-Qiang Wang<sup>a</sup> and Chun-Guang Liu<sup>a</sup>

The electrochemical reduction reaction of CO<sub>2</sub> (CO<sub>2</sub>RR) to C<sub>2+</sub> products is strongly related to the C–C coupling reaction. In general, deoxidation productions of CO<sub>2</sub> have been assigned as the active species for the C–C coupling reaction. For example, the direct coupling of two \*CO, \*CO and \*CHO, and two \*CHO species are always proposed to be the three main pathways for the formation of the C–C bond in CO<sub>2</sub>RR. In this case, a direct coupling of two inert CO<sub>2</sub> molecules to form a CO<sub>2</sub> dimer with strong C–C bond over the Cu<sup>0</sup> atomic interfaces of the Cu<sub>4</sub> cluster, which was anchored on a nitrogen-doped graphene support (Cu<sub>4</sub>/N<sub>3</sub>GN), has been proposed based on our periodic density functional theory (DFT) calculations. The mechanistic investigation shows that the atomic interface formed by the three Cu<sup>0</sup> species of Cu<sub>4</sub>/N<sub>3</sub>GN can simultaneously adsorb two CO<sub>2</sub> molecules, and two adsorbed CO<sub>2</sub> molecules could be reduced to a CO<sub>2</sub><sup>–</sup> anionic radical with [O=C=O]<sup>–</sup> configuration *via* an electron-transfer process from the three Cu<sup>0</sup> species to the two adsorbed CO<sub>2</sub> molecules. Furthermore, the direct coupling of two CO<sub>2</sub><sup>–</sup> anionic radicals results in the formation of a C–C bond. The calculated free energy profiles reveal that the direct coupling of two CO<sub>2</sub> molecules should be the main reaction relevant to the coupling of \*OCHO and CO, \*COOH and \*CO, and two CO molecules over the catalyst surface. Electronic structural analysis indicates that the bent arrangement of two adsorbed CO<sub>2</sub> molecules is a key factor in the determination of the formation of the C–C bond in the CO<sub>2</sub> dimer *via* effective orbital interactions. In addition, the CO<sub>2</sub> dimer could be reduced to ethane in the series of electrochemical elementary steps. The high ethane selectivity of the Cu<sub>4</sub>/N<sub>3</sub>GN catalyst studied here mainly arises from the strong Cu–O bonding interaction. Regarding the direct coupling of two inert CO<sub>2</sub> molecules over the atomic interface of the Cu<sub>4</sub> cluster, these findings would be very useful to guide the search for potential catalysts for the formation of the C–C bond in CO<sub>2</sub>RR into the subnanometer cluster with various active sites.

Received 29th September 2023,  
Accepted 1st November 2023

DOI: 10.1039/d3qi02000b

[rsc.li/frontiers-inorganic](http://rsc.li/frontiers-inorganic)

## 1. Introduction

Subnanometer copper (Cu)-based clusters have received considerable attention in the conversion of CO<sub>2</sub> to valuable chemicals because of their unique electronic structure and excellent catalytic performance.<sup>1–6</sup> Compared with bulk Cu surfaces and large Cu-based nanoparticles, subnanometer Cu-based clusters possess a larger surface-to-volume ratio and more active sites.<sup>7</sup> Owing to the high surface energy, they have several advantages in the adsorption of the inert

CO<sub>2</sub> molecule. The adsorption and activation of the CO<sub>2</sub> molecule by catalysts is the first step for the conversion of CO<sub>2</sub> to any valuable chemicals.<sup>8,9</sup> An activated CO<sub>2</sub> molecule, which has the lengthening of the C–O bond and the bending of the O–C–O bond angle, is always generated from an efficient electron-transfer process between catalysts and the CO<sub>2</sub> molecule.<sup>10–12</sup> For this purpose, the oxidation state of the active Cu cluster has been well investigated by using experimental and theoretical methods. It has been reported that the ionic form of Cu<sup>+</sup> was the active center for the activation of CO<sub>2</sub> molecule by the Cu-based clusters,<sup>13–15</sup> however, other investigations suggested that the measured Cu<sup>0</sup> species is strongly correlated to the activation of CO<sub>2</sub> molecule.<sup>16–18</sup> Meanwhile, the cluster size and support composition are also key factors in the determination of the catalytic activity for the reported subnanometer Cu-based clusters.<sup>19–22</sup> To date, a clear assignment of the active Cu

<sup>a</sup>Department of Chemistry, Faculty of Science, Beihua University, Jilin City, 132013, P. R. China. E-mail: liucg407@163.com; Tel: +86 043264606919

<sup>b</sup>Institute of Functional Material Chemistry, Faculty of Chemistry, Northeast Normal University, Changchun 130024, P. R. China

† Electronic supplementary information (ESI) available. See DOI: <https://doi.org/10.1039/d3qi02000b>

site has not been achieved yet, and is still under debate for the subnanometer Cu-based clusters.

Recently, several theoretical and experimental studies have been reported for the reduction of  $\text{CO}_2$  to methanol/ethanol catalyzed by a four-atom Cu cluster ( $\text{Cu}_4$ ) on the surface of various supports.<sup>23–25</sup> Liu and co-workers reported that a carbon-supported  $\text{Cu}_n$  ( $n = 3, 4$ ) cluster achieved a single-product faradaic efficiency (FE) of 91% at  $-0.71$  V (*versus* the reversible hydrogen electrode).<sup>26</sup> The FE of ethanol was found to be closely associated with the initial dispersion of Cu atoms. In their density functional theory (DFT) calculations, a supported  $\text{Cu}_3$  cluster was assigned as a model to probe the possible reaction mechanism, assuming a  $\text{Cu}_4$  cluster would share the similar mechanism. They found that the  $\text{HCOOH}^*$  intermediate was reduced to  $\text{CH}_3^* + \text{H}_2\text{CO}^*$ , which underwent a C–C bond formation to form ethanol. Alternatively, the conventional  $\text{CO}^*$  pathway was found to have a higher reaction free energy in several steps than the  $\text{HCOO}^*$  pathway. In another case, the same group reported that a size-selected  $\text{Cu}_4$  cluster is the most active low-pressure catalyst for the reduction of  $\text{CO}_2$  to methanol.<sup>27</sup> DFT calculations showed that the unsaturated Cu sites in the  $\text{Cu}_4$  clusters resulted in a strong adsorption of the adsorbates, which leads to an energetically low-lying reaction pathway. A systematic study of the size and support effects was carried out by using X-ray adsorption spectroscopy, catalytic activity measurement, and DFT calculations. They found that the catalytic activity for methanol synthesis varied strongly as a function of the Cu cluster size. The  $\text{Cu}_4/\text{Al}_2\text{O}_3$  catalyst shows the highest turnover rate for methanol among all reported catalysts.<sup>27,28</sup> By contrast, the  $\text{Cu}_3/\text{Al}_2\text{O}_3$  catalyst showed less than 50% activity because the stronger charge transfer interaction with  $\text{Al}_2\text{O}_3$  support for  $\text{Cu}_3$  than  $\text{Cu}_4$  leads to a less favorable energetic pathway for the reduction of  $\text{CO}_2$  to methanol.<sup>27</sup> In addition to methanol and ethanol, the  $\text{Cu}_4$  cluster was found to be an efficient catalyst for the conversion of  $\text{CO}_2$  to CO and acetylene trimerization.<sup>29</sup> Rodriguez *et al.* reported that a small  $\text{Cu}_4$  cluster in contact with  $\text{TiC}(001)$  displays a very high activity for the conversion of  $\text{CO}_2$  to CO.<sup>30</sup> DFT calculations showed that the  $\text{Cu}_4/\text{TiC}(001)$  catalyst can bind  $\text{CO}_2$  well, with the adsorption energy of  $-25.6$  kcal  $\text{mol}^{-1}$ , which is about 2 times as large as that of the  $\text{Cu}_9/\text{TiC}(001)$  catalyst ( $-13.6$  kcal  $\text{mol}^{-1}$ ). Schlexer and co-workers found that the interaction between the  $\text{Cu}_4$  cluster and a silica-surfaces can be enhanced by introduction of the hydroxyl groups,<sup>31</sup> whereas the dopants have only a small effect on the interaction. Meanwhile, the possible reaction mechanism of acetylene trimerization catalyzed by the silica-supported  $\text{Cu}_4$  cluster has been probed based on their DFT calculations. All of these instructive studies showed that (i) the catalytic activity of the  $\text{Cu}_4$  clusters is unique and relevant to its analogues, such as  $\text{Cu}_3$ ,  $\text{Cu}_9$ ,  $\text{Cu}_{13}$  and  $\text{C}_{29}$  clusters, *etc.*; (ii) the reactivity of the  $\text{Cu}_4$  cluster may be tuned in a desired manner by the support composition; (iii) the active Cu site in the  $\text{Cu}_4$  cluster is strongly sensitive to the interaction between the  $\text{Cu}_4$  clusters and support surfaces. These

factors encouraged us to probe the potential catalytic properties of the  $\text{Cu}_4$  cluster for  $\text{C}_2$  product synthesis.

Nitrogen-doped carbon materials have attracted considerable attention in the field of  $\text{CO}_2\text{RR}$  because of their adjustable pore structure, high specific surface area, and good electrochemical stability.<sup>32–37</sup> Especially in the study of M–N–C catalysts based on metal elements such as Cu, Ni, Fe, and Co, *etc.*, it has been demonstrated that these catalysts have high activity and selectivity for the reduction of  $\text{CO}_2$  to CO.<sup>38–42</sup> Among the various reported metals, the carbon-loaded Cu-based catalyst shows high activity in  $\text{CO}_2\text{RR}$ .<sup>43–46</sup> These reported catalysts are of particular interest because of their ability to generate large amounts of hydrocarbons, including  $\text{HCOOH}$ ,  $\text{CH}_4$ ,  $\text{C}_2\text{H}_4$ , *etc.*<sup>47–51</sup> Shen and co-workers found that the anchoring of Cu atoms on defective diamond graphene results in excellent catalytic performance for the selective conversion of acetylene to ethylene.<sup>52</sup> Baturina *et al.* reported that introduction of the Cu atomic chains into nitrogen-doped carbon materials can break the scaling relationship by providing secondary adsorption sites, thus effectively reducing the overpotential of the electrocatalytic reduction of  $\text{CO}_2$  to methanol.<sup>53</sup> Shi and co-workers proposed that the morphology of the carbon support has a significant effect on the catalytic performance of these Cu-based materials in  $\text{CO}_2\text{RR}$ .<sup>54</sup> They found that the selectivity for  $\text{CO}_2\text{RR}$  is very sensitive to the carbon support morphologies. An onion-like carbon support can effectively improve the stability, activity, and selectivity for the reduction of  $\text{CO}_2$  to  $\text{C}_2\text{H}_4$ .<sup>55</sup> DFT calculations show that the defect site of the nitrogen-doped carbon support not only promotes the electron transport to the key intermediate corresponding to the potential limiting step, but also prevents the sintering of Cu atoms because the defect sites can bind the Cu atom with the strong Cu–N bonding interaction.<sup>56,57</sup>

In previous investigations, the formation of the C–C bond in  $\text{CO}_2\text{RR}$  generally comes from the coupling reactions between two deoxidation productions of  $\text{CO}_2$ , such as the direct coupling of two  $^*\text{CO}$  species, direct coupling of the  $^*\text{CO}$  and  $^*\text{CHO}$  species, and direct coupling of two  $^*\text{CHO}$  species.<sup>28,58–61</sup> In this case, a direct coupling of two inert  $\text{CO}_2$  molecules to form a  $\text{CO}_2$  dimer with a C–C bond over the atomic interface of the  $\text{Cu}_4$  cluster, which was anchored on a nitrogen-doped graphene substrate ( $\text{Cu}_4/\text{N}_3\text{GN}$ ), has been proposed based on our DFT calculations. Our mechanistic investigation shows that the atomic interface formed by the three  $\text{Cu}^0$  species of  $\text{Cu}_4/\text{N}_3\text{GN}$  can simultaneously adsorb two  $\text{CO}_2$  molecules. The two adsorbed  $\text{CO}_2$  molecules were firstly reduced to a  $\text{CO}_2^{\cdot-}$  anionic radical with  $[\text{O}=\text{C}^{\cdot}=\text{O}]^-$  configuration *via* an electron-transfer process from the three  $\text{Cu}^0$  species of  $\text{Cu}_4/\text{N}_3\text{GN}$  catalyst to the two adsorbed  $\text{CO}_2$  molecules. The direct coupling of the two  $\text{CO}_2^{\cdot-}$  anionic radicals then resulted in the formation of a  $\text{CO}_2$  dimer with a C–C bond. Furthermore, the produced  $\text{CO}_2$  dimer could be reduced to ethane in the series of electrochemical elementary steps. This study provided a new mechanism for the formation of the C–C bond, and shed light on further improving the  $\text{CO}_2\text{RR}$  catalysts through the rational design of a subnanometer Cu-based catalyst.

## 2. Computation details

All of the first-principles calculations are based on DFT<sup>62</sup> to calculate the Perdew–Burke–Ernzerhof (PBE) functional and projector augmented wave (PAW)<sup>63,64</sup> pseudopotential using the generalized gradient approximation (GGA)<sup>65</sup> realized in the Vienna *ab initio* simulation program (VASP).<sup>66,67</sup> For all graphene supporting structures, a  $6 \times 6 \times 1$  original graphene supercell was used for the doping of nitrogen atoms and loading of metal clusters, and the geometrically optimized convergence threshold was set to an effective 0.03 eV Å<sup>-1</sup>. The cutoff energy of the plane wave basis group is 500 eV. In order to prevent the interaction between periodic images along the z-direction, the vacuum of 26.7 Å is used for the flat plate calculation, and a dipole correction is applied. The Brillouin zone of the surface is sampled with the Monkhorst–K point grid of  $2 \times 2 \times 1$   $\gamma$  center, while only  $\gamma$  points are sampled for molecular calculations and higher  $7 \times 7 \times 1$  for the projected density of states (pDOS) calculations.<sup>68</sup> The climbing image miniature elastic band method is used to calculate the transition state (TS).<sup>69,70</sup> Some atomic charges are calculated by the Bader charge analysis method.<sup>71</sup>

The computational hydrogen electrode (CHE) method was applied in free energy diagrams, which assumes that half of the free energy of gaseous hydrogen is equivalent to the free energy of a proton–electron pair at 0 V, all pH values, and 1 atm. Thus, the energy of H<sub>2</sub>(g) is used as an electrochemical ref. 72 The adsorption energy ( $E_{\text{ad}}$ ) is obtained from the following formula:

$$E_{\text{ad}} = E_{\text{total}} - E_{\text{slab}} - E_{\text{adsorbate}}.$$

Among them,  $E_{\text{total}}$  represents the total energy of the catalyst surface adsorbed by the adsorption species,  $E_{\text{slab}}$  represents the surface energy of the catalysts without the adsorption species, and  $E_{\text{adsorbate}}$  represents the energy of the adsorption species. Therefore, the more negative the adsorption energy, the stronger the adsorption capacity. The binding energy ( $E_b$ ) was calculated as:

$$E_b = E_{\text{AB}} - E_A - E_B$$

where  $E_{\text{AB}}$  denotes the total energy of the whole system of the catalyst,  $E_A$  denotes the energy of the Cu<sub>4</sub> cluster, and  $E_B$  denotes the energy of the nitrogen-doped carbon graphene carrier. The Gibbs free energy ( $\Delta G$ ) is modified by the VASPkit<sup>73</sup> program at 298 K and 100 kPa,<sup>74</sup> as follows:

$$\Delta G = E_{\text{DFT}} + \Delta \text{ZPE} - \text{TS}$$

$$\Delta \text{ZPE} = \sum i \frac{1}{2} \hbar \nu_i$$

where  $\hbar$  is the Planck constant,  $\nu_i$  is the calculated actual frequency of the system, and  $E_{\text{DFT}}$  is the calculated total energy. The total entropy ( $S$ ) is calculated from ref. 75

The frequency of the optimized adsorption species at  $\gamma$  point is determined by the VASP method, and the convergence accuracy is improved. When calculating the frequency of the

adsorbent, the whole catalyst system is fixed and only the adsorbent is released. For the free energy correction of adsorbed matter, VASPkit attributes the contribution of vibration to the translational or rotational part; in other words, the 3N vibration of the surface-adsorbed molecules (except the imaginary frequency) is used to calculate the correction of the thermal energy. In addition, the solvation program VASPsol was used to implicitly describe the effects of electrolytes and solvents.<sup>76</sup> The solvent molecule was regarded as a continuous medium model, and the dielectric constant ( $\epsilon = 78.4$ ) was used to express the solvent. In this work, the free energy of all isomers, intermediates, transition state (TS), and products along the reaction pathways was calculated in the solvent.

## 3. Results and discussion

### 3.1. Geometric and electronic structure of Cu<sub>4</sub>/N<sub>3</sub>GN catalyst

In order to ascertain the adsorption and activation of CO<sub>2</sub> by the Cu<sub>4</sub>/N<sub>3</sub>GN catalyst, we first need to determine the stable structure of the Cu<sub>4</sub>/N<sub>3</sub>GN catalyst. In the present paper, all of the possible structures of the initial geometries for the Cu<sub>4</sub> cluster, which already were reported recently in the literature for a study of the adsorption of CO<sub>2</sub> on Cu-based clusters, have been considered.<sup>77,78</sup>

As shown in Fig. 1, our periodic DFT calculations obtained five possible geometric arrangements as anchoring of these Cu<sub>4</sub> clusters onto the nitrogen-doped graphene supports (1, 2, 3, 4, and 5). Based on these optimized geometries, we calculated the free energy of these isomers (see Fig. 1). The calculated relative free energy of these isomers increased in the following order: 4 (0.00 eV) < 1 (0.19 eV) < 2 (0.21 eV) < 5 (5.80 eV) < 3 (10.92 eV), indicating that the most stable species comes from anchoring the Cu<sub>4</sub> cluster with a rhombus-like structure onto the nitrogen-doped graphene supports, in which one Cu atom residing at the vertices of the rhombus-like structure coordinates to the three nitrogen atoms of the nitrogen-doped graphene support. The second higher energy isomer for the Cu<sub>4</sub> cluster is an inverted-tetrahedron-like structure, and is only 0.19 eV higher in energy than the lowest energy isomer optimized with the PBE functional. The third higher energy isomer is found to be another rhombus-like structure for the anchored Cu<sub>4</sub> cluster, which is only 0.21 eV higher in energy than the most stable isomer.

To further evaluate the stability of the Cu<sub>4</sub>/N<sub>3</sub>GN catalyst, we carried out calculations of the binding energy ( $E_b$ ) between the Cu<sub>4</sub> cluster and nitrogen-doped graphene supports. The calculated  $E_b$  value of all possible isomers also has been compared in Fig. 1. It can be found that the calculated  $E_b$  value increases in the following order: 1 (-2.68 eV) < 4 (-1.77 eV) < 2 (-1.45 eV) < 3 (-0.58 eV) < 5 (2.66 eV). The negative  $E_b$  value indicates a strong interaction of the Cu<sub>4</sub> cluster and nitrogen-doped graphene supports, and thus a good stability. Thus, the isomer 1 with inverted-tetrahedron-like structure possesses the strongest interaction of the Cu<sub>4</sub> cluster and nitrogen-doped graphene supports among all isomers for the Cu<sub>4</sub>/N<sub>3</sub>GN cata-

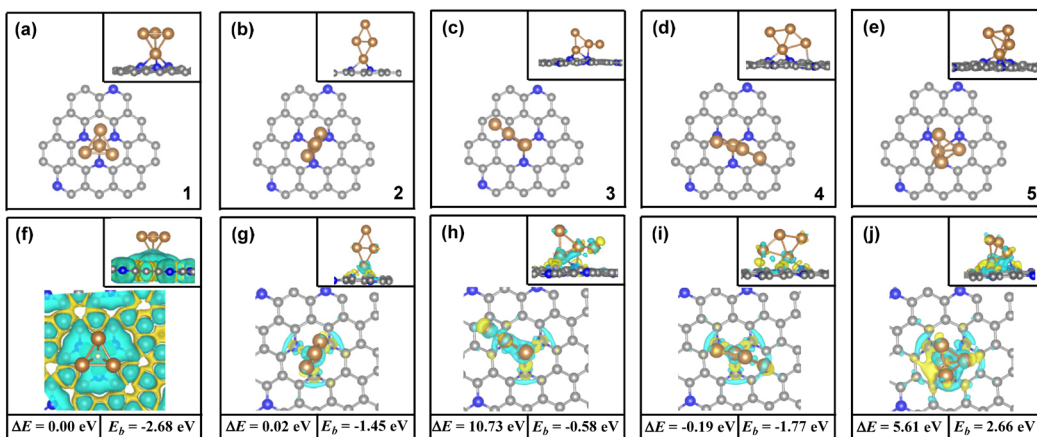


**Fig. 1** The geometric arrangement and charge density difference of all possible isomers for the  $\text{Cu}_4/\text{N}_3\text{GN}$  catalysts studied here, where the calculated relative free energy of these isomers and binding energy of the  $\text{Cu}_4$  cluster and nitrogen-doped graphene support also have been compared. ((a) and (f) for 1, (b) and (g) for 2, (c) and (h) for 3, (d) and (i) for 4, (e) and (j) for 5.).

ysts studied here. The calculated  $E_b$  value of the inverted-tetrahedron-like isomer is about two times as large as that for the two rhombus-like isomers 2 and 4 ( $-2.68$  vs.  $-1.45$  and  $-1.77$  eV). Our optimization calculations also provide the same results, in which the average Cu–N bond length of the inverted-tetrahedron-like isomer is optimized to be shorter than that of the two rhombus-like isomers ( $2.00$  vs.  $2.04$  Å and  $2.01$  Å). Meanwhile, the Bader charge analysis shows that the charges of the coordinated Cu atom binding to the three N atoms in the inverted-tetrahedron-like isomer is about  $-0.57e$ . Furthermore, the charge density difference shows that electrons accumulate on the three N atoms and adjacent C atoms on the support surface of the inverted-tetrahedron-like isomer 1, which indicates an electron-transfer process from the coordinated Cu atom to the nitrogen-doped graphene support. Moreover, the extra electrons were entirely delocalized over the surface of nitrogen-doped graphene support. Such delocalized effects effectively improve the stability of the  $\text{Cu}_4/\text{N}_3\text{GN}$  catalyst. Meanwhile, these results support a donor–acceptor bonding interaction of the coordinated Cu atom and the nitrogen-doped graphene supports in the inverted-tetrahedron-like isomer. By the same logic, the donor–acceptor bonding interaction also can be found in two rhombus-like isomers. The charge density difference also shows that electrons accumulate between the three N atoms and coordinated Cu atom in the two rhombus-like isomers. However, no delocalization effects of the extra electrons have been observed on the nitrogen-doped graphene supports in the rhombus-like isomers. Thus, the stability of both isomers is not better than that of the inverted-tetrahedron-like isomer. All of these results indicate that the strong interaction of the  $\text{Cu}_4$  cluster with the inverted-tetrahedron-like structure and the nitrogen-doped graphene substrate experimentally provide good feasibility in terms of synthesis of the  $\text{Cu}_4/\text{N}_3\text{GN}$  catalyst. We will focus on the inverted-tetrahedron-like isomer in the following discussions.

### 3.2. Adsorption and activation of $\text{CO}_2$ over the $\text{Cu}_4/\text{N}_3\text{GN}$ catalyst

In the inverted-tetrahedron-like isomer, the four Cu atoms are tightly coupled through metal bonds to form a cluster (see ESI Table S1†). One Cu atom in the  $\text{Cu}_4$  cluster is anchored to the defects of the nitrogen-doped graphene substrate, and interacts with the three N atoms on the substrate. The calculated Bader charge of the Cu atoms, which does not directly attach to the N atom, is about zero (see ESI Table S2†). Thus, the  $\text{Cu}_4$  cluster in the inverted-tetrahedron-like isomer may be described as a  $\text{Cu}^+ \text{Cu}^0_3$  configuration, in which the three  $\text{Cu}^0$  species form an atomic interface over the  $\text{Cu}_4$  cluster. The transition metal center in a lower oxidation state always displays stronger ability to bind the adsorbates, according to previous investigations. Furthermore, the atomic interface formed by the unsaturated three  $\text{Cu}^0$  species in the  $\text{Cu}_4/\text{N}_3\text{GN}$  catalyst may have the ability to interact with molecules. Thus, they should be viewed as potential sites for the adsorption and activation of the inert  $\text{CO}_2$  molecule. The effective combination of three possible  $\text{Cu}^0$  sites may adsorb one or two  $\text{CO}_2$  molecules over the surface of the  $\text{Cu}_4/\text{N}_3\text{GN}$  catalyst.

For the adsorption of the first  $\text{CO}_2$  molecule, our DFT calculations provide three possible adsorption configurations (top, bridge\_1, and bridge\_2 models). For the top model, the  $\text{CO}_2$  molecule was adsorbed on the top of three  $\text{Cu}^0$  sites, in which the C and two O atoms of the  $\text{CO}_2$  molecule directly interact with three  $\text{Cu}^0$  sites. Meanwhile, in the bridge\_1 model, the  $\text{CO}_2$  molecule was localized at a position between two Cu atoms, in which two O atoms of the  $\text{CO}_2$  molecule directly interact with the two  $\text{Cu}^0$  sites. On the other hand, in the bridge\_2 model, the C atom and one O atom of the  $\text{CO}_2$  molecule directly interact with two  $\text{Cu}^0$  sites.

In order to identify the stability of these adsorption configurations, the adsorption energy ( $E_{\text{ad}}$ ) has been calculated by using our DFT calculations. The calculated  $E_{\text{ad}}$  values also have been compared in Fig. 2. It was found that the calculated

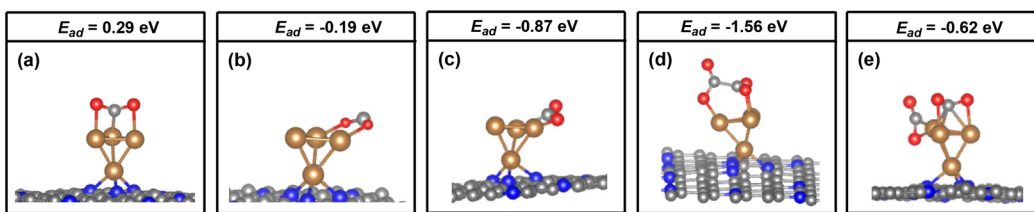


**Fig. 2** The key geometric parameters and adsorption energy analysis of the possible adsorption configuration of the  $\text{CO}_2$  molecule on the  $\text{Cu}_4/\text{N}_3\text{GN}$  catalyst with the (a) top, (b) bridge\_1, (c) bridge\_2, (d) coupling and (e) isolating models.

$E_{\text{ad}}$  value increases in the following order:  $E_{\text{ad}}$  (bridge\_2) ( $-0.87 \text{ eV}$ )  $< E_{\text{ad}}$  (bridge\_1) ( $-0.19 \text{ eV}$ )  $< E_{\text{ad}}$  (top) ( $0.01 \text{ eV}$ ), indicating a strong adsorption of  $\text{CO}_2$  on the  $\text{Cu}_4/\text{N}_3\text{GN}$  catalyst in the bridge\_2 model. By contrast, the calculated  $E_{\text{ad}}$  values of the top and bridge\_1 model are both higher than bridge\_2, indicating that both adsorption configurations are not stable species. Such results indicate that the two  $\text{Cu}^0$  sites in the most stable adsorption configuration (bridge\_2) are not occupied as the adsorption of the first  $\text{CO}_2$  molecule, which is available for adsorption of the second  $\text{CO}_2$  molecule.

For the adsorption of the second  $\text{CO}_2$  molecule, two possible adsorption configurations have been obtained (coupling and isolating models). The most stable configuration is found to be the coupling model (see Fig. 2d), in which the three O atoms of the two  $\text{CO}_2$  molecules direct interact with the three  $\text{Cu}^0$  sites. Meanwhile, a direct coupling of two adsorbed  $\text{CO}_2$  molecules to form a  $\text{CO}_2$  dimer with a C-C bond length of  $1.55 \text{ \AA}$  has been found, according to our optimization calculations. The calculated  $E_{\text{ad}}$  value of the coupling model is about  $0.94 \text{ eV}$  lower in energy than that of the isolating model ( $-1.56 \text{ vs. } -0.62 \text{ eV}$ ). It is well known that the selectivity of the catalyst to the  $\text{C}_{2+}$  products in  $\text{CO}_2\text{RR}$  is closely related to the formation of C-C bonds. According to previous reports, the formation of the C-C bond arises from three major pathways, including the \*CO dimerization, \*CO and \*CHO dimerization, and \*CHO dimerization over the catalyst surface. However, the direct coupling of two inert  $\text{CO}_2$  molecules to form a  $\text{CO}_2$  dimer with the strong C-C bond has not been found over the Cu-based catalysts. Interestingly, as shown in Fig. 2d, our optimization calculations provide a unique geometric arrangement, in which the two adsorbed  $\text{CO}_2$  molecules are bound to each other *via* a strong C-C single bond over the atomic interface of the  $\text{Cu}_4/\text{N}_3\text{GN}$  catalyst. Such results strongly suggest a direct coupling of two inert  $\text{CO}_2$  molecules to form a  $\text{CO}_2$  dimer over the atomic interface of the  $\text{Cu}_4/\text{N}_3\text{GN}$  catalyst.

### 3.3. $\text{CO}_2$ dimerization

Electrochemical reduction of  $\text{CO}_2$  is a very complicated system. The  $\text{CO}_2$  molecule could be reduced to \*OCHO, \*COOH, \*CO, \*CHO, \*CH, and \*CH<sub>2</sub>, and others in the series of electrochemical elementary steps, which would become the potential coupling species for the formation of the C-C bond in  $\text{CO}_2\text{RR}$ .<sup>49,79,80</sup> These species may occupy the active sites of the catalyst and suppress the direct coupling of two  $\text{CO}_2$  molecules

over the surface of the  $\text{Cu}_4/\text{N}_3\text{GN}$  catalyst. Owing to the low surface concentrations of \*CHO, \*CH, \*CH<sub>2</sub>, and other multiple reduced species of  $\text{CO}_2$  molecule over the catalytic surface, the reaction pathway for the coupling of these species to form the C-C bond is not important when compared with the high concentration species \*CO<sub>2</sub>, \*OCHO, \*COOH, and \*CO. In the present paper, starting from the \*CO<sub>2</sub>, \*OCHO, \*COOH, and \*CO species, all possible coupling reactions for the combination of these species have been considered. According to our optimization calculations, four possible coupling pathways have been obtained. The calculated free energy curves for these reaction pathways are shown in Fig. 3.

It was found that the calculated free energy curve for the direct coupling of two \*CO<sub>2</sub> molecules is located at the bottom, and has the lowest free energy barrier. By contrast, the calculated free energy curves of the direct coupling of two CO molecules are located in a third high-energy place, in which the calculated free energy barrier is about  $0.62 \text{ eV}$  higher in energy than that of the direct coupling of two CO<sub>2</sub> molecules. The calculated relative energy of the CO dimer is about  $0.84 \text{ eV}$  higher in energy than that of the CO<sub>2</sub> dimer. Thus, the direct coupling of two CO molecules over the surface of the  $\text{Cu}_4/\text{N}_3\text{GN}$  catalyst is both thermodynamically and kinetically unfavorable when compared with that of the two CO<sub>2</sub> molecules. As shown in Fig. 3, the calculated free energy curve of the coupling of \*CO and \*OCHO is located at the top, and has the highest energy barrier among them. Thus, such coupling reaction is not significant both thermodynamically and kinetically. Although the calculated free energy curve for the coupling of \*CO and \*COOH is located in a second high-energy place, the calculated free energy barrier is about 2 times as high as that of the direct coupling of two CO<sub>2</sub> molecules ( $0.94 \text{ vs. } 0.52 \text{ eV}$ ). Thus, the competition effects of this coupling reaction may not be significantly relevant to the direct coupling of two CO<sub>2</sub> molecules. All these results indicate that the direct coupling of two CO<sub>2</sub> molecules over the surface of the  $\text{Cu}_4/\text{N}_3\text{GN}$  catalyst could be the main reaction for the formation of the C-C bond in the complicated electrochemical system.

The optimized geometric arrangements of the key transition states and intermediates for the direct coupling of two CO<sub>2</sub> molecules are shown in Fig. 3. It was found that the two CO<sub>2</sub> molecules firstly approach the three  $\text{Cu}^0$  species to form an adsorption complex \*CO<sub>2</sub> + \*CO<sub>2</sub> (isolating models). In \*CO<sub>2</sub> + \*CO<sub>2</sub>, the optimized O<sub>2</sub>C-CO<sub>2</sub> distance is  $3.355 \text{ \AA}$ ,

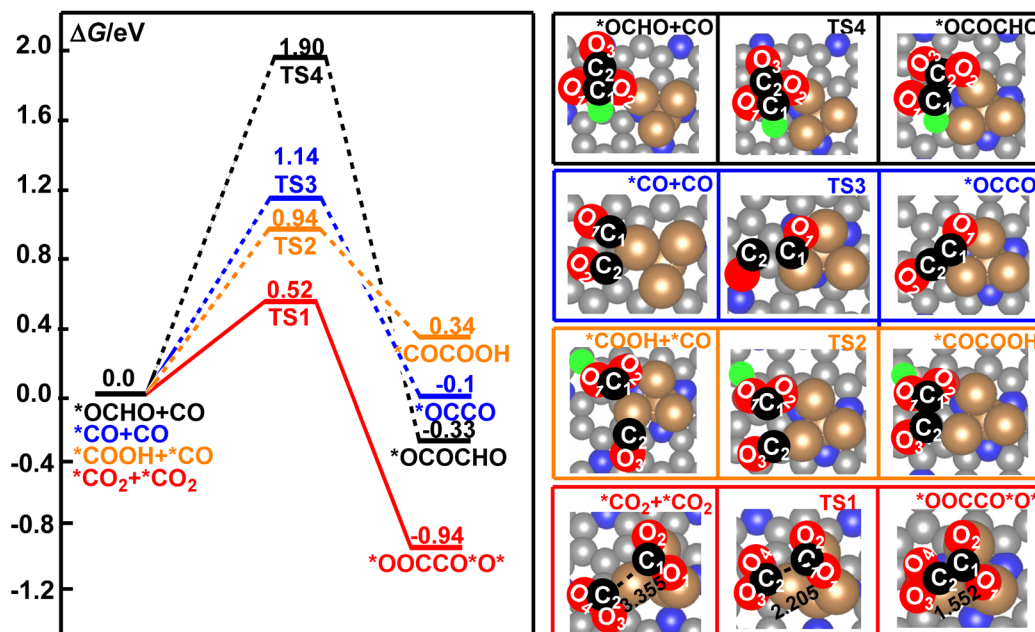
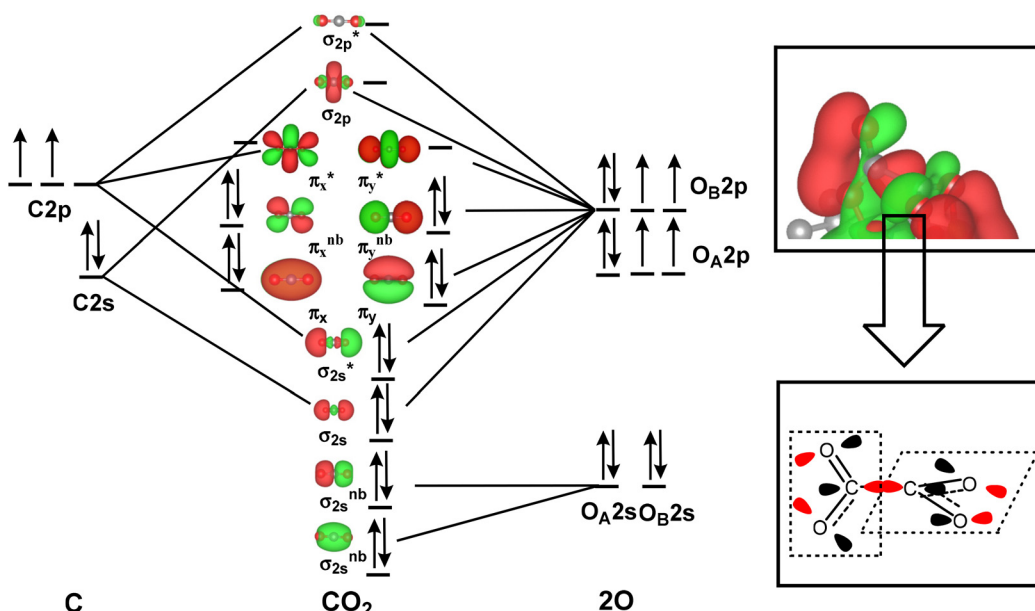


Fig. 3 The calculated free energy profiles for the direct coupling of two  $\text{CO}_2$ ,  $\text{OCHO}$  and  $\text{CO}$ ,  $\text{COOH}$  and  $\text{CO}$ , and two  $\text{CO}$  molecules to form a C–C bond on the surface of the  $\text{Cu}_4/\text{N}_3\text{GN}$  catalyst.

indicating a very weak interaction between the two  $\text{CO}_2$  molecules over the surface of the  $\text{Cu}_4/\text{N}_3\text{GN}$  catalyst. The calculated Bader charge of the two adsorbed  $\text{CO}_2$  molecules is +0.78 e and +0.49 e in  $\text{CO}_2 + \text{CO}_2$ , respectively. The calculated Bader charge of the three Cu atoms in  $\text{CO}_2 + \text{CO}_2$ , which are not attached to the N atom of the nitrogen-doped graphene substrate, is -0.25, -0.44, and -0.25 e, respectively. The calculated Bader charge of the Cu atom coordinated to the three N atoms of the nitrogen-doped graphene substrate is -0.46 e in  $\text{CO}_2 + \text{CO}_2$ . Compared with the neutral  $\text{CO}_2$  molecule and  $\text{Cu}_4$  cluster with  $\text{Cu}^+ - \text{Cu}_3^0$  configuration on the clear surface of the  $\text{Cu}_4/\text{N}_3\text{GN}$  catalyst, such results indicate that the two adsorbed  $\text{CO}_2$  molecules have been activated *via* an electron-transfer process from three  $\text{Cu}^0$  species in the  $\text{Cu}_4$  cluster of the  $\text{Cu}_4/\text{N}_3\text{GN}$  catalyst to the two adsorbed  $\text{CO}_2$  molecules. Thus, the two  $\text{CO}_2$  moieties in  $\text{CO}_2 + \text{CO}_2$  have been reduced and possess the bent structure with elongated C–O bond length relative to the free  $\text{CO}_2$  molecule, and can be viewed as two  $\text{CO}_2^-$  anionic radicals. A detailed analysis of the calculated Bader charge shows that the C atom is -2.10, -1.38, and -1.61 e for the free  $\text{CO}_2$  molecule and two adsorbed  $\text{CO}_2$  molecules, respectively. The calculated Bader charge of the two O atoms is (1.05 and 1.05 e), (1.08 and 1.08 e), and (1.04 and 1.06 e) for the free and two adsorbed  $\text{CO}_2$  molecules, respectively. Such results indicate that the reduced electrons are mainly localized on the C atom adjacent to the O atoms for the two adsorbed  $\text{CO}_2$  molecules in this electron-transfer process ( $\Delta q(\text{C}) = 0.72$  and 0.49 e for the two adsorbed  $\text{CO}_2$  molecules in this electron-transfer process, respectively). Thus, the electron configuration of the two adsorbed  $\text{CO}_2$  molecules should be described as  $[\text{O}=\text{C}^{\cdot-}=\text{O}]^-$ . The C atom of the two adsorbed

$\text{CO}_2$  molecules would significantly contribute to the formation of a C–C single bond in the process of  $\text{CO}_2$  dimerization. Then, our optimization calculation shows the direct coupling of two anionic  $\text{CO}_2$  radicals with  $[\text{O}=\text{C}^{\cdot-}=\text{O}]^-$  configuration over the  $\text{Cu}_4/\text{N}_3\text{GN}$  catalyst *via* TS1, which needs an activation energy of 0.52 eV with an imaginary frequency of  $244.83 \text{ cm}^{-1}$ . At TS1, the  $\text{O}_2\text{C} \cdots \text{CO}_2$  distance was shortened to 2.205 Å, indicating that a new bond may form between the two adsorbed  $\text{CO}_2$  molecules. In TS1, the calculated Bader charge of the two C atoms in the adsorbed two  $\text{CO}_2$  molecules is -1.47 and -1.72 e, respectively, compared with the Bader charge of the C atoms in free  $\text{CO}_2$  (-2.10 e), indicating the distinct radical feature for the two adsorbed  $\text{CO}_2$  molecules in TS1. After TS1, the two  $\text{CO}_2$  anionic radicals come together to form a  $\text{CO}_2$  dimer,  $\text{OOC}\text{CO}^{\cdot*}$ , over the  $\text{Cu}_4/\text{N}_3\text{GN}$  catalyst. This coupling process is calculated to be exoergic by 0.94 eV, indicating that  $\text{OOC}\text{CO}^{\cdot*}$  has a high thermodynamic stability. Furthermore, the direct coupling of two  $\text{CO}_2$  molecule over the surface of  $\text{Cu}_4/\text{N}_3\text{GN}$  catalyst has a large thermodynamic driving force. All of these results indicate that the  $\text{CO}_2$  dimerization reaction over the  $\text{Cu}_4/\text{N}_3\text{GN}$  catalyst should be viewed as a free-radical-coupling reaction.

As mentioned above, the two adsorbed  $\text{CO}_2$  molecules over the atomic interface of  $\text{Cu}_4/\text{N}_3\text{GN}$  catalyst were reduced and possess bent structure. The reduced electron is mainly localized over the C atom of the adsorbed  $\text{CO}_2$  molecule, according to the Bader charge analysis. The frontier molecular orbitals (FMOs) of the free  $\text{CO}_2$  molecule are listed in Fig. 4. It can be seen that the two degenerated LUMOs of the free  $\text{CO}_2$  molecule consist of 2p orbitals of the C atom and two O atoms with  $\pi^*$  antibonding feature, and mainly localized over the C atom



**Fig. 4** The frontier molecular orbitals of free carbon dioxide molecules and the HOMO of the  $^*\text{OOC*O*}$  dimer, highlighting that the effective overlapping of two distorted  $\pi^*$  antibonding orbitals of two bent  $\text{CO}_2$  molecules results in the formation of the C–C bond in the  $\text{CO}_2$  dimer.

adjacent to the O atoms. Thus, injection of extra electrons into the LUMOs would localize on the C atom of the  $\text{CO}_2$  molecule, which are in good agreement with our Bader charge analysis.

Meanwhile, our electronic structural analysis shows that  $^*\text{OOC*O*}$  provided a unique molecular orbital topology for the formation of the C–C bond in the  $\text{CO}_2$  dimer. As shown in Fig. 4, our optimization calculations show that the two adsorbed  $\text{CO}_2$  molecules with bent structure definite two planes, in which the dihedral angle of the two planes is calculated to be  $121.9^\circ$ . Such geometric arrangement could effectively avoid the repulsion effects from the O atoms of the  $\text{CO}_2$  molecule, and make the two C atoms of the adsorbed  $\text{CO}_2$  molecules get closer in the process of  $\text{CO}_2$  dimerization. The molecular orbital topology (HOMO) of  $^*\text{OOC*O*}$  represents the C–C bonding interaction. It can be seen that HOMO could be viewed as an effective overlapping of two distorted  $\pi^*$  antibonding orbitals of the  $\text{CO}_2$  molecule. The bent arrangement of the adsorbed  $\text{CO}_2$  molecule leads to a mixing of 2p orbitals of the two O atoms in the  $\text{CO}_2$  molecule, which effectively polarizes the 2p orbital of the C atom in the  $\text{CO}_2$  molecule. The polarized 2p orbital of the C atom promotes the overlapping of two distorted  $\pi^*$  antibonding orbitals, and significantly contributes to the formation of the C–C bond in the  $\text{CO}_2$  dimer. All of these results indicate that the bent arrangement of the  $\text{CO}_2$  molecule is the key factor in the determination of the formation of the C–C bond *via* effective orbital interactions.

The nature of the  $\text{CO}_2$  dimer,  $^*\text{OOC*O*}$ , is a key factor in the determination of the formation of the  $\text{C}_2$  product in  $\text{CO}_2\text{RR}$ . As shown in Fig. 5, the four oxygen atoms in  $^*\text{OOC*O*}$  are the potential sites in the following elementary steps. In the present paper, we firstly considered the possible dissociated products of  $^*\text{OOC*O*}$  *via* cleavage of the four

C–O bonds, respectively. The calculated relative energy of the four dissociated products has been compared in Fig. 5. It can be found that the calculated relative energy of the four dissociated products increases in the following order:  $\text{O}_3$  (0.34 eV) <  $\text{O}_2$  (0.48 eV) <  $\text{O}_4$  (0.82 eV) <  $\text{O}_1$  (1.28 eV), indicating that these four dissociated processes are all endergonic. Furthermore, the most stable species among them comes from dissociation of the  $\text{O}_3$  atom from the  $^*\text{OOC*O*}$  intermediate to form a  $^*\text{OCCOO*}$  species and a remaining  $^*\text{O}$  species. Owing to the high thermodynamic stability of  $^*\text{OOC*O*}$ , this dissociated process is calculated to have a high free energy barrier of 1.75 eV. However, this high barrier can be compensated by the following reduction reaction of the remaining  $^*\text{O}$  species to  $\text{H}_2\text{O}$  over the  $\text{Cu}_4/\text{N}_3\text{GN}$  catalyst.

After TS5, the  $\text{O}_3$  atom moves from the top site of the Cu atom into the bridge site between the two Cu atoms. Meanwhile, the dissociated fragment of  $^*\text{OCCOO*}$  was bound over the surface of the  $\text{Cu}_4/\text{N}_3\text{GN}$  catalyst *via* a new Cu–C<sub>2</sub> bond and a Cu–O<sub>2</sub> bond. The remaining  $\text{O}_3$  atom would be reduced to  $\text{H}_2\text{O}$  and leave the surface of the  $\text{Cu}_4/\text{N}_3\text{GN}$  catalyst. Although a lot of efforts have been made, we did not find any rational geometric arrangement for the hydrogenation of  $^*\text{OOC*O*}$ . As shown in Fig. 3, three out of the four oxygen atoms in  $^*\text{OOC*O*}$  were bound to the three Cu atoms of the  $\text{Cu}_4/\text{N}_3\text{GN}$  catalyst *via* three strong Cu–O bonds. Thus, the three O atoms are located in the Cu–O–C units and in the chemical saturated states. Such structural arrangement of the three O atoms significantly weakens the reactivity with the proton–electron pairs. The  $\text{O}_4$  atom, which was bound to the  $^*\text{OOC*O*}$  *via* a C<sub>2</sub>–O<sub>4</sub> bond, also cannot react with the proton–electron pair to form a hydrogenation product because of the weak reactivity. All of these results indicate that the con-

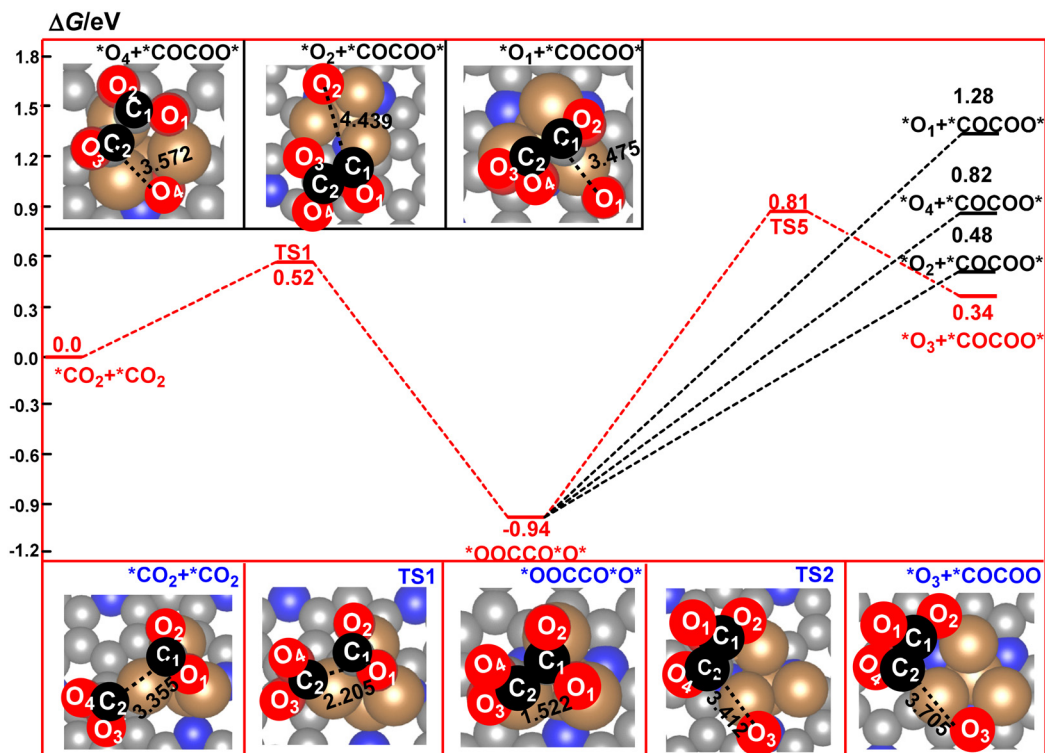


Fig. 5 Calculated reaction pathways for the formation and decomposition of the  $\text{CO}_2$  dimer on the surface of the  $\text{Cu}_4/\text{N}_3\text{GN}$  catalyst.

versation of the stable  $^*\text{OOCOO}^*\text{O}^*$  to  $^*\text{OCCOO}^*$  over the surface of the  $\text{Cu}_4/\text{N}_3\text{GN}$  catalyst could be triggered by a heating process because dissociation of the stable  $\text{CO}_2$  dimer is an endergonic process with a high free energy barrier. By contrast, implementing of the electroreduction process at room temperature may not produce the  $\text{C}_2$  product for our studied system in this work.

#### 3.4. Formation of ethane

In previous literature, the number of oxygen atoms in the C–C coupling product is up to two, such as  $^*\text{OCCO}$ .<sup>81,82</sup> In general, the proton–electron pair preferentially attacks at the O atom of the C–C coupling product because of the high basicity of the O atom relative to the C atom.<sup>82,83</sup> Thus, the nature of the O atom in the C–C coupling product would significantly affect the selectivity of the catalyst in  $\text{CO}_2\text{RR}$ . For our studied system, the decomposition product of the  $\text{CO}_2$  dimer,  $^*\text{O}_3 + ^*\text{OCCOO}^*$ , contains four O atoms. The possible reaction pathways corresponding to the generation of the  $\text{C}_2$  products entirely differ from the reported mechanism. The calculated free energy profiles of the whole reaction pathway for the hydrogenation of  $^*\text{O}_3 + ^*\text{OCCOO}^*$  to ethane is shown in Fig. 6 and 7. All of the O sites of the  $^*\text{O}_3 + ^*\text{OCCOO}^*$  intermediate have been considered for the first hydrogenation step. As expected, the reduction of the  $^*\text{O}_3$  atom to a  $^*\text{OH}$  group is calculated to be energetically much more favorable among them. According to our free energy calculations, hydrogenation of  $^*\text{O}_3 + ^*\text{OCCOO}^*$  to the  $^*\text{COCOO}^* + ^*\text{OH}$  intermediate is calculated to be exoergic by

1.19 eV, indicating that the  $^*\text{COCOO}^* + ^*\text{OH}$  intermediate is a thermodynamically stable species, and will remain on the catalyst surface long enough for further reduction to  $\text{H}_2\text{O}$ .

For the second reduction step, the hydrogenation of the  $^*\text{COCOO}^* + ^*\text{OH}$  intermediate to  $^*\text{COCOO}^* + ^*\text{H}_2\text{O}$  is calculated to be exoergic by 0.29 eV. Next, desorption of the produced  $\text{H}_2\text{O}$  molecules from the catalyst surface to form a  $^*\text{COCOO}^*$  intermediate is calculated to be endergonic by 0.72 eV.

Subsequently, the proton–electron pair preferentially attacks at the  $\text{C}_2$  atom of  $^*\text{COCOO}^*$ , which binds to the Cu atom, to generate  $^*\text{CHOCOO}^*$  intermediates with a free energy downhill of 0.12 eV. This step leads to a complete cleavage of the Cu– $\text{C}_2$  bond, and the  $\text{CHOCOO}^*$  moiety was bound to the catalyst surface *via* a Cu– $\text{O}_2$  bond. Owing to the strong Cu– $\text{O}_2$  bonding interaction, the hydrogenation of the  $\text{O}_2$  site in the conversion from  $^*\text{COCOO}^*$  to  $^*\text{COCOOH}$  is calculated to be energetically unfavorable. Then, the proton–electron pair preferentially attacks at the  $\text{O}_4$  atom of  $^*\text{CHOCOO}^*$  to produce  $^*\text{CHOHCOO}^*$  with a free energy downhill of 0.41 eV. The optimized Cu– $\text{O}_2$  bond length increases from 1.892 Å in  $^*\text{CHOCOO}^*$  to 1.896 Å in  $^*\text{CHOHCOO}^*$ , indicating that this hydrogenation step does not largely affect the Cu– $\text{O}_2$  bonding interaction. In the following two hydrogenated steps, the  $^*\text{CHOHCOO}^*$  was hydrogenated to form  $\text{CH}_2\text{OHCOHO}^*$  with two exothermic steps by 0.18 and 0.48 eV, respectively. For the thermodynamically unstable  $\text{CH}_2\text{OHCOHO}^*$  species, it was immediately hydrogenated to form the second  $\text{H}_2\text{O}$  molecule in  $\text{CH}_3\text{COO}^* + \text{H}_2\text{O}$  over the  $\text{Cu}_4/\text{N}_3\text{GN}$  catalyst. This hydrogen-

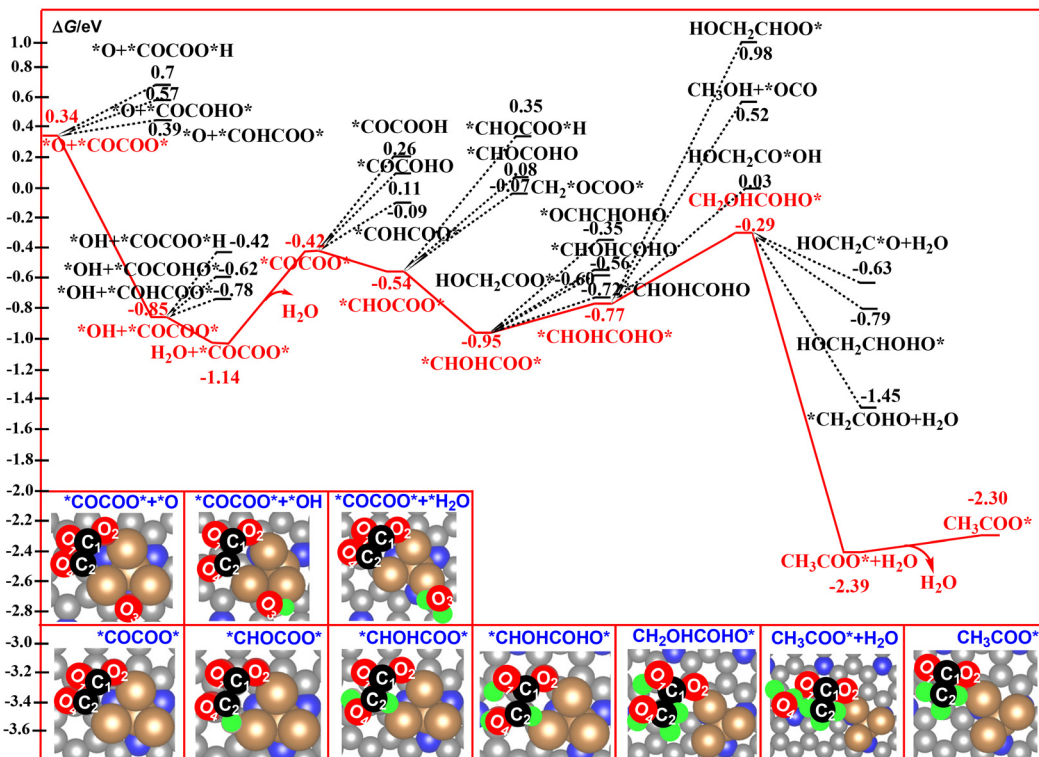


**Fig. 6** Calculated free energy profiles for the electrocatalytic reduction of  $^{*}\text{O}_3 + ^{*}\text{OCCOO}^{*}$  to  $\text{CH}_3\text{COO}^{*}$ .

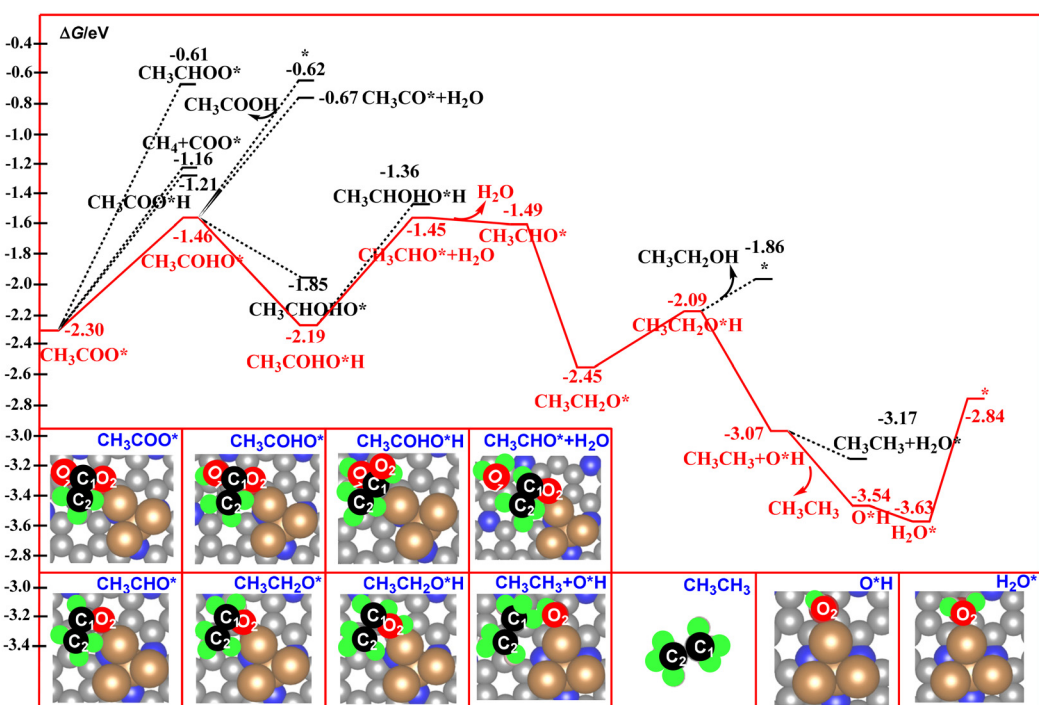


**Fig. 7** Calculated free energy profiles for the electrocatalytic reduction of  $\text{CH}_3\text{COO}^*$  to acetic acid, ethanol, and ethane.

ation step is calculated to be most exoergic by 2.10 eV among all of the reaction steps studied here. Desorption of the second  $\text{H}_2\text{O}$  molecule from the catalyst surface leads to the formation

of  $\text{CH}_3\text{COO}^*$ . The calculated desorption energy for this process is 0.09 eV, indicating a very weak interaction of the produced  $\text{H}_2\text{O}$  molecule and the catalyst surface.

For the  $\text{CH}_3\text{COO}^*$  intermediate, it could be reduced to  $\text{CH}_3\text{COOH}$  *via* hydrogenation of the  $\text{O}_2$  atom. As shown in Fig. 7, the  $\text{C}_2$  atom in  $\text{CH}_3\text{COO}^*$  is in a saturated state *via* formation of three C–H bonds and one C–C bond. Thus, the  $\text{O}_1$ ,  $\text{O}_2$ , and  $\text{C}_1$  atoms have been assigned as the potential sites for the reaction with the proton–electron pairs. According to our free energy calculations, hydrogenation of the  $\text{O}_1$  atom to form  $\text{CH}_3\text{COHO}^*$  is much more favorable compared to the  $\text{O}_2$  and  $\text{C}_1$  atoms.

This step is calculated to be exoergic by 0.84 eV. By contrast, hydrogenation of the  $\text{O}_2$  atom to form a  $\text{CH}_3\text{COOH}$  molecule over the catalyst surface is calculated to be exoergic by 1.09 eV, and the release of the produced  $\text{CH}_3\text{COOH}$  molecule from the catalyst surface *via* cleavage of the  $\text{Cu}–\text{O}_2$  bond needs a desorption energy of 0.59 eV. Such results indicate that the strong  $\text{Cu}–\text{O}_2$  bonding interaction suppresses the formation of the  $\text{CH}_3\text{COOH}$  molecule. By contrast, the continuous hydrogenation of the  $\text{CH}_3\text{COHO}^*$  to  $\text{CH}_3\text{COHO}^*\text{H}$  is a favorable path, in which this step is calculated to be exoergic by 0.73 eV. Next, hydrogenation of  $\text{CH}_3\text{COHO}^*\text{H}$  to  $\text{CH}_3\text{CHO}^* + \text{H}_2\text{O}$  results in the formation of the third  $\text{H}_2\text{O}$  molecule over the catalyst surface with a free energy downhill of 0.74 eV. After desorption of the third  $\text{H}_2\text{O}$  molecule from the catalyst surface, a  $\text{CH}_3\text{CHO}^*$  intermediate is formed with a free energy downhill of 0.04 eV. Further the hydrogeneration of  $\text{CH}_3\text{CHO}^*$  results in the formation of the  $\text{CH}_3\text{CH}_2\text{O}^*$  intermediate with a free energy downhill of 0.96 eV. For the  $\text{CH}_3\text{CH}_2\text{O}^*$  intermediate, the hydrogeneration of the  $\text{O}_2$  atom of the  $\text{CH}_3\text{CH}_2\text{O}^*$  intermediate would produce the  $\text{CH}_3\text{CH}_2\text{OH}$  molecule. This step is calculated to be exoergic by 0.36 eV. For the  $\text{CH}_3\text{CH}_2\text{O}^*\text{H}$  intermediate, the pathway bifurcates into ethanol- and ethane-forming routes. As shown in Fig. 7, the releasing of the  $\text{CH}_3\text{CH}_2\text{OH}$  molecule *via* cleavage of the  $\text{Cu}–\text{O}_2$  bond is found to be more unfavorable than the formation of the ethane molecule in  $\text{CH}_3\text{CH}_3 + *\text{OH}$ , as the calculated free energy of the former is 1.21 eV higher than that of the latter. Furthermore, desorption of the  $\text{CH}_3\text{CH}_3$  molecule from the catalyst surface is calculated to be exoergic by 0.47 eV. These results indicate that ethane is the main product of direct  $\text{CO}_2$  reduction catalyzed by the  $\text{Cu}_4/\text{N}_3\text{GN}$  catalyst. Furthermore, the hydrogeneration of the produced  $^*\text{OH}$  group results in the formation of the fourth  $\text{H}_2\text{O}$  molecule with a free energy downhill of 0.09 eV. Finally, the catalyst was resumed *via* release of the fourth  $\text{H}_2\text{O}$  with a free energy uphill of 0.79 eV. In the whole reaction pathway, the potential-limiting step is still the decomposition of the  $\text{CO}_2$  dimer to  $^*\text{O} + ^*\text{OCCOO}^*$  with an energy of 1.75 eV, which is lower than the direct coupling of two CO on the Cu (111) surface (1.81 eV). Thus, the  $\text{Cu}_4/\text{N}_3\text{GN}$  catalyst possesses excellent catalytic activity and high ethane selectivity for direct  $\text{CO}_2$  reduction.

## 4. Conclusions

We have systematically investigated the nitrogen-doped graphene-supported  $\text{Cu}_4$  cluster with various structures. Our

optimization calculations show that anchoring the  $\text{Cu}_4$  cluster with an inverted-tetrahedron-like structure onto the nitrogen-doped graphene supports results in a catalyst with strong interaction between them, which provides high feasibility in terms of the experimental synthesis of the catalyst. The electronic structure analysis shows that the atomic interface of the inverted-tetrahedron-like  $\text{Cu}_4$  cluster possesses a  $\text{Cu}^+–\text{Cu}_3^0$  configuration. Furthermore, the three unsaturated  $\text{Cu}^0$  species in the  $\text{Cu}_4$  cluster are the potential sites for the adsorption and activation of the  $\text{CO}_2$  molecules. Our optimization and free energy calculations reveal that the adsorption of two  $\text{CO}_2$  molecules over the catalyst surface results in a direct coupling of two inert  $\text{CO}_2$  molecules to form a  $\text{CO}_2$  dimer with a strong C–C bond. The calculated free energy profiles show that the  $\text{CO}_2$  dimerization should be the main reaction relevant to the coupling reaction of  $^*\text{OCHO}$  and  $\text{CO}$ ,  $^*\text{COOH}$  and  $^*\text{CO}$ , and two  $\text{CO}$  molecules. The mechanistic investigation shows that the two adsorbed  $\text{CO}_2$  molecules were firstly reduced to  $\text{CO}_2^{\cdot-}$  anionic radicals with  $[\text{O}=\text{C}^{\cdot}=\text{O}]^{\cdot-}$  configuration *via* an electron transfer process from the surface  $\text{Cu}^0$  species to the two  $\text{CO}_2$  molecules. Furthermore, the direct coupling of two anionic radicals,  $\text{CO}_2^{\cdot-}$ , results in the formation of the C–C bond in the  $\text{CO}_2$  dimer. The orbital analysis indicates that the bent arrangement of the  $\text{CO}_2$  molecule effectively promotes the overlap of two distorted  $\pi^*$  antibonding orbitals, which significantly contribute to the formation of the C–C bond in the  $\text{CO}_2$  dimer. The free energy calculation shows that the  $\text{CO}_2$  dimer could be reduced to ethane in the series of electrochemical elementary steps. The high ethane selectivity of the  $\text{Cu}_4/\text{N}_3\text{GN}$  catalyst mainly arises from the strong  $\text{Cu}–\text{O}$  bonding interaction. This study calls for more fundamental investigations on the mechanism for the formation of the C–C bond in  $\text{CO}_2\text{RR}$ .

## Conflicts of interest

The authors declare no competing financial interest.

## Acknowledgements

The authors gratefully acknowledge the financial support from the National Natural Science Foundation of China (32130073, 21373043) and National Natural Science Foundation of Jilin Province (YDZJ202201ZYTS540).

## References

- 1 H. Zhang, Y. Yang, Y. Liang, J. Li, A. Zhang, H. Zheng, Z. Geng, F. Li and J. Zeng, Molecular Stabilization of Sub-Nanometer Cu Clusters for Selective  $\text{CO}_2$  Electromethanation, *ChemSusChem*, 2022, **15**, e202102010.
- 2 H. Dai, H. Zou, T. Song, L. Gao, S. Wei, H. Liu, H. Xiong, C. Huang and L. Duan, Pyridyl-Containing Graphdiyne Stabilizes Sub-2 nm Ultrasmall Copper Nanoclusters for

the Electrochemical Reduction of CO<sub>2</sub>, *Inorg. Chem. Front.*, 2023, **10**, 2189–2196.

3 H. Xiong, A. K. Datye and Y. Wang, Thermally Stable Single-Atom Heterogeneous Catalysts, *Adv. Mater.*, 2021, **33**, 2004319.

4 B. Zhang, Y. Chen, J. Wang, H. Pan and W. Sun, Supported Sub-Nanometer Clusters for Electrocatalysis Applications, *Adv. Funct. Mater.*, 2022, **32**, 2202227.

5 C. Liu, B. Yang, E. Tyo, S. Seifert, J. DeBartolo, B. von Issendorff, P. Zapol, S. Vajda and L. A. Curtiss, Carbon Dioxide Conversion to Methanol over Size-Selected Cu<sub>4</sub> Clusters at Low Pressures, *J. Am. Chem. Soc.*, 2015, **137**, 8676–8679.

6 S. Vajda, M. J. Pellin, J. P. Greeley, C. L. Marshall, L. A. Curtiss, G. A. Ballentine, J. W. Elam, S. Catillon-Mucherrie, P. C. Redfern and F. Mehmood, Subnanometre Platinum Clusters as Highly Active and Selective Catalysts for the Oxidative Dehydrogenation of Propane, *Nat. Mater.*, 2009, **8**, 213–216.

7 G. Sun, A. N. Alexandrova and P. Sautet, Structural Rearrangements of Subnanometer Cu Oxide Clusters Govern Catalytic Oxidation, *ACS Catal.*, 2020, **10**, 5309–5317.

8 M. Favaro, H. Xiao, T. Cheng, W. A. Goddard III, J. Yano and E. J. Crumlin, Subsurface Oxide Plays a Critical Role in CO<sub>2</sub> Activation by Cu (111) Surfaces to Form Chemisorbed CO<sub>2</sub>, the First Step in Reduction of CO<sub>2</sub>, *Proc. Natl. Acad. Sci. U. S. A.*, 2017, **114**, 6706–6711.

9 X. Su, X.-F. Yang, Y. Huang, B. Liu and T. Zhang, Single-Atom Catalysis toward Efficient CO<sub>2</sub> Conversion to CO and Formate Products, *Acc. Chem. Res.*, 2018, **52**, 656–664.

10 A. Mazheika, Y.-G. Wang, R. Valero, F. Viñes, F. Illas, L. M. Ghiringhelli, S. V. Levchenko and M. Scheffler, Artificial-Intelligence-Driven Discovery of Catalyst Genes with Application to CO<sub>2</sub> Activation on Semiconductor Oxides, *Nat. Commun.*, 2022, **13**, 419.

11 W. Tu, Y. Zhou and Z. Zou, Photocatalytic Conversion of CO<sub>2</sub> into Renewable Hydrocarbon Fuels: State-of-the-Art Accomplishment, Challenges, and Prospects, *Adv. Mater.*, 2014, **26**, 4607–4626.

12 N. Aguilar, M. Atilhan and S. Aparicio, Single Atom Transition Metals on MoS<sub>2</sub> Monolayer and Their Use as Catalysts for CO<sub>2</sub> Activation, *Appl. Surf. Sci.*, 2020, **534**, 147611.

13 L. Yuan, S.-F. Hung, Z.-R. Tang, H. M. Chen, Y. Xiong and Y.-J. Xu, Dynamic Evolution of Atomically Dispersed Cu Species for CO<sub>2</sub> Photoreduction to Solar Fuels, *ACS Catal.*, 2019, **9**, 4824–4833.

14 A. R. Woldu, Z. Huang, P. Zhao, L. Hu and D. Astruc, Electrochemical CO<sub>2</sub> Reduction (CO<sub>2</sub>RR) to Multi-Carbon Products over Copper-Based Catalysts, *Coord. Chem. Rev.*, 2022, **454**, 214340.

15 P. De Luna, R. Quintero-Bermudez, C.-T. Dinh, M. B. Ross, O. S. Bushuyev, P. Todorović, T. Regier, S. O. Kelley, P. Yang and E. H. Sargent, Catalyst Electro-Redeposition Controls Morphology and Oxidation State for Selective Carbon Dioxide Reduction, *Nat. Catal.*, 2018, **1**, 103–110.

16 H. Xiao, W. A. Goddard III, T. Cheng and Y. Liu, Cu Metal Embedded in Oxidized Matrix Catalyst to Promote CO<sub>2</sub> Activation and CO Dimerization for Electrochemical Reduction of CO<sub>2</sub>, *Proc. Natl. Acad. Sci. U. S. A.*, 2017, **114**, 6685–6688.

17 Y. Zhou, F. Che, M. Liu, C. Zou, Z. Liang, P. De Luna, H. Yuan, J. Li, Z. Wang and H. Xie, Dopant-Induced Electron Localization Drives CO<sub>2</sub> Reduction to C<sub>2</sub> Hydrocarbons, *Nat. Chem.*, 2018, **10**, 974–980.

18 J. A. Rodriguez, P. Liu, D. J. Stacchiola, S. D. Senanayake, M. G. White and J. G. Chen, Hydrogenation of CO<sub>2</sub> to Methanol: Importance of Metal–Oxide and Metal–Carbide Interfaces in the Activation of CO<sub>2</sub>, *ACS Catal.*, 2015, **5**, 6696–6706.

19 A. G. Saputro, A. L. Maulana, F. Fathurrahman, G. Shukri, M. H. Mahyuddin, M. K. Agusta, T. D. K. Wungu and H. K. Diponoro, Density Functional and Microkinetic Study of CO<sub>2</sub> Hydrogenation to Methanol on Subnanometer Pd Cluster Doped by Transition Metal (M = Cu, Ni, Pt, Rh), *Int. J. Hydrogen Energy*, 2021, **46**, 14418–14428.

20 J. Timoshenko, A. Halder, B. Yang, S. Seifert, M. J. Pellin, S. Vajda and A. I. Frenkel, Subnanometer Substructures in Nanoassemblies Formed from Clusters Under A Reactive Atmosphere Revealed Using Machine Learning, *J. Phys. Chem. C*, 2018, **122**, 21686–21693.

21 M. Gallego, A. Corma and M. Boronat, Influence of the Zeolite Support on the Catalytic Properties of Confined Metal Clusters: A Periodic DFT Study of O<sub>2</sub> Dissociation on Cu<sub>n</sub> Clusters in CHA, *Phys. Chem. Chem. Phys.*, 2022, **24**, 30044–30050.

22 A. Halder, C. Lenardi, J. Timoshenko, A. Mravak, B. Yang, L. K. Kolipaka, C. Piazzoni, S. Seifert, V. Bonacic-Koutecky and A. I. Frenkel, CO<sub>2</sub> Methanation on Cu-cluster Decorated Zirconia Supports with Different Morphology: A Combined Experimental *in situ* GIXANES/GISAXS, *ex situ* XPS and Theoretical DFT Study, *ACS Catal.*, 2021, **11**, 6210–6224.

23 X. Su, Z. Jiang, J. Zhou, H. Liu, D. Zhou, H. Shang, X. Ni, Z. Peng, F. Yang and W. Chen, Complementary Operando Spectroscopy Identification of *in-situ* Generated Metastable Charge-Asymmetry Cu<sub>2</sub>-CuN<sub>3</sub> Clusters for CO<sub>2</sub> Reduction to Ethanol, *Nat. Commun.*, 2022, **13**, 1322.

24 X. Bai, X. Zhao, Y. Zhang, C. Ling, Y. Zhou, J. Wang and Y. Liu, Dynamic Stability of Copper Single-Atom Catalysts Under Working Conditions, *J. Am. Chem. Soc.*, 2022, **144**, 17140–17148.

25 B. Yang, X. Yu, A. Halder, X. Zhang, X. Zhou, G. R. J. Mannie, E. Tyo, M. J. Pellin, S. Seifert and D. Su, Dynamic Interplay between Copper Tetramers and Iron Oxide Boosting CO<sub>2</sub> Conversion to Methanol and Hydrocarbons under Mild Conditions, *ACS Sustainable Chem. Eng.*, 2019, **7**, 14435–14442.

26 H. Xu, D. Rebollar, H. He, L. Chong, Y. Liu, C. Liu, C.-J. Sun, T. Li, J. V. Muntean and R. E. Winans, Highly Selective Electrocatalytic CO<sub>2</sub> Reduction to Ethanol by Metallic Clusters Dynamically Formed from Atomically Dispersed Copper, *Nat. Energy*, 2020, **5**, 623–632.

27 B. Yang, C. Liu, A. Halder, E. C. Tyo, A. B. Martinson, S. N. Seifert, P. Zapol, L. A. Curtiss and S. Vajda, Copper Cluster Size Effect in Methanol Synthesis from  $\text{CO}_2$ , *J. Phys. Chem. C*, 2017, **121**, 10406–10412.

28 J. Chen, Z. Wang, J. Zhao, L. Ling, R. Zhang and B. Wang, The Active Site of Ethanol Formation from Syngas over  $\text{Cu}_4$  Cluster Modified  $\text{MoS}_2$  Catalyst: A Theoretical Investigation, *Appl. Surf. Sci.*, 2021, **540**, 148301.

29 Y. Sun, S. Wang, J. Jia, Y. Liu, Q. Cai and J. Zhao, Supported  $\text{Cu}_3$  Clusters on Graphitic Carbon Nitride as An Efficient Catalyst for CO Electroreduction to Propene, *J. Mater. Chem. A*, 2022, **10**, 14460–14469.

30 J. A. Rodriguez, J. Evans, L. Feria, A. B. Vidal, P. Liu, K. Nakamura and F. Illas,  $\text{CO}_2$  Hydrogenation on  $\text{Au}/\text{TiC}$ ,  $\text{Cu}/\text{TiC}$ , and  $\text{Ni}/\text{TiC}$  Catalysts: Production of CO, Methanol, and Methane, *J. Catal.*, 2013, **307**, 162–169.

31 F. Maleki, P. Schlexer and G. Pacchioni, Support Effects and Reaction Mechanism of Acetylene Trimerization over Silica-Supported  $\text{Cu}_4$  Clusters: A DFT Study, *Surf. Sci.*, 2018, **668**, 125–133.

32 I. C. Gerber and P. Serp, A Theory/Experience Description of Support Effects in Carbon-Supported Catalysts, *Chem. Rev.*, 2019, **120**, 1250–1349.

33 T. Tang, Z. Wang and J. Guan, Electronic Structure Regulation of Single-Site MNC Electrocatalysts for Carbon Dioxide Reduction, *Acta Phys.-Chim. Sin.*, 2022, **39**, 10–3866.

34 Y. Jiang, Y. Lu, X. Lv, D. Han, Q. Zhang, L. Niu and W. Chen, Enhanced Catalytic Performance of Pt-Free Iron Phthalocyanine by Graphene Support for Efficient Oxygen Reduction Reaction, *ACS Catal.*, 2013, **3**, 1263–1271.

35 T. Wang, Q. Zhao, Y. Fu, C. Lei, B. Yang, Z. Li, L. Lei, G. Wu and Y. Hou, Carbon-Rich Nonprecious Metal Single Atom Electrocatalysts for  $\text{CO}_2$  Reduction and Hydrogen Evolution, *Small Methods*, 2019, **3**, 1900210.

36 W. Ju, A. Bagger, G.-P. Hao, A. S. Varela, I. Sinev, V. Bon, B. R. Cuenya, S. Kaskel, J. Rossmeisl and P. Strasser, Understanding Activity and Selectivity of Metal-Nitrogen-Doped Carbon Catalysts for Electrochemical Reduction of  $\text{CO}_2$ , *Nat. Commun.*, 2017, **8**, 944.

37 A. Azoulay, A. G. Baldovi, J. Albero, N. Azaria, J. Tzadikov, A. Tashakory, N. Karjule, S. Hayun, H. García and M. Shalom, Carbon-Phosphorus-Nitrogen Materials as Highly Thermally Stable Catalyst Supports for  $\text{CO}_2$  Hydrogenation to Methanol, *ACS Appl. Energy Mater.*, 2022, **6**, 439–446.

38 Y. Yang, Y. Yang, Z. Pei, K.-H. Wu, C. Tan, H. Wang, L. Wei, A. Mahmood, C. Yan and J. Dong, Recent Progress of Carbon-Supported Single-Atom Catalysts for Energy Conversion and Storage, *Matter*, 2020, **3**, 1442–1476.

39 T. Tang, Z. Wang and J. Guan, Optimizing the Electrocatalytic Selectivity of Carbon Dioxide Reduction Reaction by Regulating the Electronic Structure of Single-Atom M–N–C Materials, *Adv. Funct. Mater.*, 2022, **32**, 2111504.

40 M. Jia, C. Choi, T.-S. Wu, C. Ma, P. Kang, H. Tao, Q. Fan, S. Hong, S. Liu and Y.-L. Soo, Carbon-Supported Ni Nanoparticles for Efficient  $\text{CO}_2$  Electroreduction, *Chem. Sci.*, 2018, **9**, 8775–8780.

41 X. Li, W. Bi, M. Chen, Y. Sun, H. Ju, W. Yan, J. Zhu, X. Wu, W. Chu and C. Wu, Exclusive  $\text{Ni}-\text{N}_4$  Sites Realize Near-Unity CO Selectivity for Electrochemical  $\text{CO}_2$  Reduction, *J. Am. Chem. Soc.*, 2017, **139**, 14889–14892.

42 L.-Y. Xiao, Z. Wang and J. Guan, Optimization Strategies of High-Entropy Alloys for Electrocatalytic Applications, *Chem. Sci.*, 2023, DOI: [10.1039/D3SC04962K](https://doi.org/10.1039/D3SC04962K).

43 N. M. Julkapli and S. Bagheri, Graphene Supported Heterogeneous Catalysts: An Overview, *Int. J. Hydrogen Energy*, 2015, **40**, 948–979.

44 Y. Li, B. Wei, M. Zhu, J. Chen, Q. Jiang, B. Yang, Y. Hou, L. Lei, Z. Li and R. Zhang, Synergistic Effect of Atomically Dispersed  $\text{Ni}-\text{Zn}$  Pair Sites for Enhanced  $\text{CO}_2$  Electroreduction, *Adv. Mater.*, 2021, **33**, 2102212.

45 F. Li, H. Wen and Q. Tang, Reaction Mechanism and Kinetics for Carbon Dioxide Reduction on Iron–Nickel Bi-Atom Catalysts, *J. Mater. Chem. A*, 2022, **10**, 13266–13277.

46 S. Wang, L. Li, J. Li, C. Yuan, Y. Kang, K. S. Hui, J. Zhang, F. Bin, X. Fan and F. Chen, High-Throughput Screening of Nitrogen-Coordinated Bimetal Catalysts for Multielectron Reduction of  $\text{CO}_2$  to  $\text{CH}_4$  with High Selectivity and Low Limiting Potential, *J. Phys. Chem. C*, 2021, **125**, 7155–7165.

47 Y. Hori, A. Murata and R. Takahashi, Formation of Hydrocarbons in the Electrochemical Reduction of Carbon Dioxide at A Copper Electrode in Aqueous Solution, *J. Chem. Soc., Faraday Trans. 1*, 1989, **85**, 2309–2326.

48 T. Tang, Z. Wang and J. Guan, Structural Optimization of Carbon-Based Diatomic Catalysts towards Advanced Electrocatalysis, *Coord. Chem. Rev.*, 2023, **492**, 215288.

49 T. Ding, X. Liu, Z. Tao, T. Liu, T. Chen, W. Zhang, X. Shen, D. Liu, S. Wang and B. Pang, Atomically Precise Dinuclear Site Active toward Electrocatalytic  $\text{CO}_2$  Reduction, *J. Am. Chem. Soc.*, 2021, **143**, 11317–11324.

50 H. Wang, G. Ren, Y. Zhao, L. Sun, J. Sun, L. Yang, T. Yu, W. Deng and L. Sun, In Silico Design of Dual-Doped Nitrogenated Graphene ( $\text{C}_2\text{N}$ ) Employed in Electrocatalytic Reduction of Carbon Monoxide to Ethylene, *J. Mater. Chem. A*, 2022, **10**, 4703–4710.

51 Y. Wang, B. J. Park, V. K. Paidi, R. Huang, Y. Lee, K.-J. Noh, K.-S. Lee and J. W. Han, Precisely Constructing Orbital Coupling-Modulated Dual-Atom Fe Pair Sites for Synergistic  $\text{CO}_2$  Electroreduction, *ACS Energy Lett.*, 2022, **7**, 640–649.

52 H. Shen, Y. Li and Q. Sun, Cu Atomic Chains Supported on  $\beta$ -Borophene Sheets for Effective  $\text{CO}_2$  Electroreduction, *Nanoscale*, 2018, **10**, 11064–11071.

53 O. Baturina, Q. Lu, F. Xu, A. Purdy, B. Dyatkin, X. Sang, R. Unocic, T. Brintlinger and Y. Gogotsi, Effect of Nanostructured Carbon Support on Copper Electrocatalytic Activity toward  $\text{CO}_2$  Electroreduction to Hydrocarbon Fuels, *Catal. Today*, 2017, **288**, 2–10.

54 Z. Shi, W. Yang, Y. Gu, T. Liao and Z. Sun, Metal-Nitrogen-Doped Carbon Materials as Highly Efficient Catalysts: Progress and Rational Design, *Adv. Sci.*, 2020, **7**, 2001069.

55 Y. Yan, L. Ke, Y. Ding, Y. Zhang, K. Rui, H. Lin and J. Zhu, Recent Advances in Cu-based Catalysts for Electroreduction of Carbon Dioxide, *Mater. Chem. Front.*, 2021, **5**, 2668–2683.

56 D.-H. Lim, J. H. Jo, D. Y. Shin, J. Wilcox, H. C. Ham and S. W. Nam, Carbon Dioxide Conversion into Hydrocarbon Fuels on Defective Graphene-Supported Cu Nanoparticles from First Principles, *Nanoscale*, 2014, **6**, 5087–5092.

57 Y. X. Duan, F. L. Meng, K. H. Liu, S. S. Yi, S. J. Li, J. M. Yan and Q. Jiang, Amorphizing of Cu Nanoparticles toward Highly Efficient and Robust Electrocatalyst for CO<sub>2</sub> Reduction to Liquid Fuels with High Faradaic Efficiencies, *Adv. Mater.*, 2018, **30**, 1706194.

58 K. Yao, J. Li, H. Wang, R. Lu, X. Yang, M. Luo, N. Wang, Z. Wang, C. Liu and T. Jing, Mechanistic Insights into OC-COH Coupling in CO<sub>2</sub> Electroreduction on Fragmented Copper, *J. Am. Chem. Soc.*, 2022, **144**, 14005–14011.

59 X. Bai and J. Guan, Applications of MXene-Based Single-Atom Catalysts, *Small Struct.*, 2023, **4**, 2200354.

60 G. M. Tomboc, S. Choi, T. Kwon, Y. J. Hwang and K. Lee, Potential Link between Cu Surface and Selective CO<sub>2</sub> Electroreduction: Perspective on Future Electrocatalyst Designs, *Adv. Mater.*, 2020, **32**, 1908398.

61 J. Li, S. U. Abbas, H. Wang, Z. Zhang and W. Hu, Recent Advances in Interface Engineering for Electrocatalytic CO<sub>2</sub> Reduction Reaction, *Nano-Micro Lett.*, 2021, **13**, 1–35.

62 R. Haunschild, A. Barth and W. Marx, Evolution of DFT Studies in View of A Scientometric Perspective, *J. Cheminf.*, 2016, **8**, 1–12.

63 G. Kresse and D. Joubert, From Ultrasoft Pseudopotentials to the Projector Augmented-Wave Method, *Phys. Rev. B: Condens. Matter Mater. Phys.*, 1999, **59**, 1758.

64 P. E. Blöchl, Projector Augmented-Wave Method, *Phys. Rev. B: Condens. Matter Mater. Phys.*, 1994, **50**, 17953.

65 J. P. Perdew, K. Burke and M. Ernzerhof, Generalized Gradient Approximation Made Simple, *Phys. Rev. Lett.*, 1996, **77**, 3865.

66 G. Kresse and J. Furthmüller, Efficiency of ab-initio Total Energy Calculations for Metals and Semiconductors Using a Plane-Wave Basis Set, *Comput. Mater. Sci.*, 1996, **6**, 15–50.

67 G. Kresse and J. Furthmüller, Efficient Iterative Schemes for ab initio Total-Energy Calculations Using A Plane-Wave Basis Set, *Phys. Rev. B: Condens. Matter Mater. Phys.*, 1996, **54**, 11169.

68 H. J. Monkhorst and J. D. Pack, Special Points for Brillouin-Zone Integrations, *Phys. Rev. B: Solid State*, 1976, **13**, 5188.

69 G. Henkelman, B. P. Uberuaga and H. Jónsson, A Climbing Image Nudged Elastic Band Method for Finding Saddle Points and Minimum Energy Paths, *J. Chem. Phys.*, 2000, **113**, 9901–9904.

70 G. Henkelman and H. Jónsson, Improved Tangent Estimate in the Nudged Elastic Band Method for Finding Minimum Energy Paths and Saddle Points, *J. Chem. Phys.*, 2000, **113**, 9978–9985.

71 E. Sanville, S. D. Kenny, R. Smith and G. Henkelman, Improved Grid-Based Algorithm for Bader Charge Allocation, *J. Comput. Chem.*, 2007, **28**, 899–908.

72 J. K. Nørskov, J. Rossmeisl, A. Logadottir, L. Lindqvist, J. R. Kitchin, T. Bligaard and H. Jonsson, Origin of the Overpotential for Oxygen Reduction at A Fuel-Cell Cathode, *J. Phys. Chem. B*, 2004, **108**, 17886–17892.

73 T. Cheng, H. Xiao and W. A. Goddard III, Full Atomistic Reaction Mechanism with Kinetics for CO Reduction on Cu (100) from ab initio Molecular Dynamics Free-Energy Calculations at 298 K, *Proc. Natl. Acad. Sci. U. S. A.*, 2017, **114**, 1795–1800.

74 V. Wang, N. Xu, J.-C. Liu, G. Tang and W.-T. Geng, VASPKIT: A pre- and Post-Processing Program for VASP Code. 2019, arXiv.org e-Print archive. <https://arxiv.org/abs/1908.08269>.

75 D. R. Lide, *CRC Handbook of Chemistry and Physics*, CRC press, 2004.

76 K. Mathew, R. Sundararaman, K. Letchworth-Weaver, T. Arias and R. G. Hennig, Implicit Solvation Model for Density-Functional Study of Nanocrystal Surfaces and Reaction Pathways, *J. Chem. Phys.*, 2014, **140**, 084106.

77 Megha, K. Mondal, T. K. Ghanty and A. Banerjee, Adsorption and Activation of CO<sub>2</sub> on Small-Sized Cu-Zr Bimetallic Clusters, *J. Phys. Chem. A*, 2021, **125**, 2558–2572.

78 X. Liang, X. Ren, M. Guo, Y. Li, W. Xiong, W. Guan, L. Gao and A. Liu, CO<sub>2</sub> Electroreduction by AuCu Bimetallic Clusters: A First Principles Study, *Int. J. Energy Res.*, 2021, **45**, 18684–18694.

79 J. Zhao, P. Zhang, T. Yuan, D. Cheng, S. Zhen, H. Gao, T. Wang, Z.-J. Zhao and J. Gong, Modulation of \*CH<sub>x</sub>O Adsorption to Facilitate Electrocatalytic Reduction of CO<sub>2</sub> to CH<sub>4</sub> over Cu-Based Catalysts, *J. Am. Chem. Soc.*, 2023, **145**, 6622–6627.

80 X. Ma, Y. Zhang, T. Fan, D. Wei, Z. Huang, Z. Zhang, Z. Zhang, Y. Dong, Q. Hong and Z. Chen, Facet Dopant Regulation of Cu<sub>2</sub>O Boosts Electrocatalytic CO<sub>2</sub> Reduction to Formate, *Adv. Funct. Mater.*, 2023, **33**, 2213145.

81 J. Yin, Z. Yin, J. Jin, M. Sun, B. Huang, H. Lin, Z. Ma, M. Muzzio, M. Shen and C. Yu, A New Hexagonal Cobalt Nanosheet Catalyst for Selective CO<sub>2</sub> Conversion to Ethanal, *J. Am. Chem. Soc.*, 2021, **143**, 15335–15343.

82 H. Bao, Y. Qiu, X. Peng, J.-A. Wang, Y. Mi, S. Zhao, X. Liu, Y. Liu, R. Cao and L. Zhuo, Isolated Copper Single Sites for High-Performance Electroreduction of Carbon Monoxide to Multicarbon Products, *Nat. Commun.*, 2021, **12**, 238.

83 F. Cai, X. Hu, F. Gou, Y. Chen, Y. Xu, C. Qi and D.-K. Ma, Ultrathin ZnIn<sub>2</sub>S<sub>4</sub> Nanosheet Arrays Activated by Nitrogen-Doped Carbon for Electrocatalytic CO<sub>2</sub> Reduction Reaction Toward Ethanol, *Appl. Surf. Sci.*, 2023, **611**, 155696.